Optimization of SOFC anode/electrolyte assembly based on BaIn$_{0.3}$Ti$_{0.7}$O$_{2.85}$ (BIT07)/Ni-BIT07 using an interfacial anodic layer

M. Benamira, M. Letilly, E. Quarez, O. Joubert, A. Le Gal La Salle*

Institut des Matériaux Jean Rouxel (IMN), CNRS-Université de Nantes, 2 rue de la Houssinière, BP 32229, 44322 Nantes, France

HIGHLIGHTS

- Anode active layers.
- Tape casting and co-sintering.
- Electrochemical performance and durability of SOFC.

ARTICLE INFO

ABSTRACT

BaIn$_{0.3}$Ti$_{0.7}$O$_{2.85}$ (BIT07) is a potential electrolyte material for Solid Oxide Fuel Cells (SOFCs) due to its high ionic conductivity and its compatibility with commonly used cathode materials. By using tape casting and co-sintering shaping methods symmetrical cells BIT07-Ni/BIT07/BIT07-Ni have been prepared. In order to improve the interface between BIT07-Ni and BIT07, a thin anode functional active layer (AAL) deposited between the BIT07-Ni and BIT07 is used. The effect of this layer on the electrochemical performance of the symmetrical cells as well as the influence of an additional Ni current collecting layer deposited on the anode side are discussed in this study. It is shown that the presence of the AAL decreases the area specific resistance (ASR) of the anode/assembly by a factor of about two, and that the presence of the Ni layer slows down the ageing of the assembly.

© 2013 Elsevier B.V. All rights reserved.

1. Introduction

Solid Oxide Fuel Cells (SOFCs) are of great interest as energy conversion devices due to their high energy efficiency and environmentally friendly behaviour [1]. Nowadays, cells operate at 800–750 °C or even higher and a decrease to less than 700 °C is expected in order to increase the life-time of the cell. In this intermediate temperature range, anode supported cells are considered with an electrolyte layer as thin as possible to limit the ohmic loss, and exhibiting a specific ionic conductivity level around 10^{-2} S cm^{-1}. According to this criterion, BaIn$_{0.3}$Ti$_{0.7}$O$_{2.85}$ (BIT07) is regarded as a potential electrolyte material [2].

Using tape casting [3,4], it is possible to prepare anode/electrolyte assemblies based on BIT07-Ni/BIT07. The anode is a cermet (ceramic–metal), i.e. a composite made of BIT07, which will provide the ionic conductivity, and of nickel, which will provide both the electronic conductivity and catalytic properties towards the hydrogen oxidation [5–10]. During its shaping step the raw anode tape is composed of BIT07 and NiO and the co-firing of the anode/electrolyte assembly is carried out in air. The cermet is obtained after the sintering step by reducing the NiO to Ni at the working temperature of the cell under reducing atmosphere.

In a previous paper [11], the anode microstructure has been optimized (porosity, phase distribution and particle size), and complete cells have been also realized. The best power densities obtained at 700 °C and 0.7 V was 336 mW cm^{-2}. In this case, the total ASR of the cell is roughly of 0.65 Ω cm^2, in which 0.38 Ω cm^2 comes from the electrodes polarization and the rest (0.27 Ω cm^2) from the current collector and electrolyte. The main part of the polarization resistance (approximately the two thirds), comes from the anode. Improvements must therefore be done in order to decrease the resistance due to the anode part. The anode must fulfil three main requirements (i) oxygen anionic conductivity, (ii) electronic conductivity and (iii) catalytic activity toward fuel oxidation. In the anode, the electrochemical reaction can only

* Corresponding author. Tel.: +33 240373913; fax: +33 240373995.
  E-mail address: annie.legal@cnrs-imn.fr (A. Le Gal La Salle).

occur at the triple phase boundary (TPB) that is the interface between the electrolyte, the electron-conducting metal phase and the gas phase. According to published works, it seems that the region in which the TPB exists extends no more than 20 μm–10 μm from the electrolyte into the electrode [12–16], and that a special attention must be brought to the electrolyte/anode interface [17,18]. In order to extend this region, some authors [3,13,14,19,20] have proposed to add intermediate layers between electrolyte and anode layers. Taking into account the previous results obtained with Ni/BIT07 cermets prepared with BIT07 and NiO in weight ratios comprised in the 30:70–50:50 range, with addition of 2.5–15 wt.% of pore-forming agent [21,22], anode/electrolyte symmetrical cells were realized by inserting an intermediary layer between the anode and the electrolyte. The anode cermet has been realized with BIT07 and NiO in a 50:50 wt. ratio, and 5 wt.% carbon black (CB) as pore-forming agent and the intermediary layer is based on BIT07 and NiO in a 45:55 wt. ratio, and 2.5 wt.% CB.

In order to further improve the anode performance, the addition of a Ni current collecting layer between the anode and the current collector has been also tested.

2. Materials and methods

2.1. Powders

BIT07 powder was synthesized by solid-state reaction as detailed in Ref. [2]: its constituents, high purity barium carbonate (Alfa Aesar), indium oxide (Alfa Aesar) and titanium dioxide (Merck), in stoichiometric ratio, were mixed in mortar and pestle using ethanol. The mixture was first heated at 1200 °C for 24 h, then ground and compacted into pellets and sintered at 1350 °C for 24 h, and finally ground and passed through mesh 100. To obtain a grain size of about one micron or less, the powder was ball-milled in 45 ml silicon nitride pot with 15 silicon nitride balls in ethanol at 500 rpm using FRITSCH P7 planetary micro mill. Nickel oxide powder, with a grain size ranged between 0.5 and 1 μm, was provided by Pharmacie Centrale de France. Carbon Black super P, the pore-forming agent, was provided by Timcal.

2.2. Preparation of symmetrical anode/electrolyte/anode assemblies

2.2.1. Slurry preparation

The anode, the AAL and the electrolyte were prepared by tape casting. First, the electrolyte (E) slurry is prepared by mixing the ball milled BIT07 powder, a dispersant (oleic acid) and an azeotropic mixture of solvents (ethanol and 2-butanon) in 45 ml silicon nitride pot with 12 silicon nitride balls at 240 rpm for 1 h. Binders (Polyvinyl Butyral PVB-90 and PVB-98) and plasticizers (Polyethylene glycol PEG-400 and dibutyl phthalate) are subsequently added to the former preparation and ball-milled for 24 h at 180 rpm [5].

Then, the anode (A) slurry is prepared by mixing NiO powder with the previous electrolyte slurry in the BIT07:NiO weight ratio of 50:50. CB was added (5 wt.% of the powder amount) to obtain porous anode material. The AAL slurry is prepared by mixing NiO and BIT07 in the weight ratio of 55:45, and adding CB in 2.5 wt.%.

2.2.2. A/E/A symmetrical cells

The anode/electrolyte (BIT07-NiO/BIT07) assembly is realized in two steps. First an electrolyte tape with a thickness of 100 μm is cast on Mylar and dried in air for one night [23], then on its surface, an anode tape with a thickness of 800 μm is deposited

and dried in air for one night. This method, named co-tape casting, allows us to obtain a bilayer anode/electrolyte noted AE [24]. Then, this bilayer is cut into two pieces and the two parts are joined so the electrolyte is face to face: AE/EA. The cohesion at the electrolyte–electrolyte interface is obtained by co-pressing the assembly. The green tape is cut in discs of 9 mm in diameter.

Finally the following thermal treatment is applied to remove slowly the organic species and to sinter the half-cell:

$$RT \overset{50K.h^{-1}}{\rightarrow} 600\ °C\ (4\ h) \overset{100K.h^{-1}}{\rightarrow} 1300\ °C\ (9\ h) \overset{100K.h^{-1}}{\rightarrow} RT$$

After sintering, an "anode" supported symmetrical cell is obtained with 100–110 μm thick anode and 20–30 μm thin electrolyte, as schematized on Fig. 1a. The surface is comprised between 0.28 and 0.45 cm^2.

2.2.3. A/AAL/E/AAL/A symmetrical cells

As described in previous section, an electrolyte tape with a thickness of 100 μm is cast on Mylar and dried in air for one night. Second, the AAL tape with a thickness of 150 μm is deposited on the surface of the electrolyte tape and dried in air for one night. Finally an anode tape (800 μm) is deposited onto the previous tapes, and dried in air for one night. This multilayer is cut into two pieces and the two parts are joined so the two electrolyte tapes are face to face and sintered as explained in Section 2.2.2.

2.2.4. TAAL/E/TAAL symmetrical cells

Other symmetrical cells have been prepared, in which the anode consists in a thick anode active layer, they are noted TAAL/E/TAAL. In this case the anode slurry corresponds to the composition of the anodic active layer AAL (NiO and BIT07 in the weight ratio of 55:45 and 2.5 wt.% of CB). The electrolyte and anode tapes are cast with respective thicknesses of 100 μm and 800 μm.
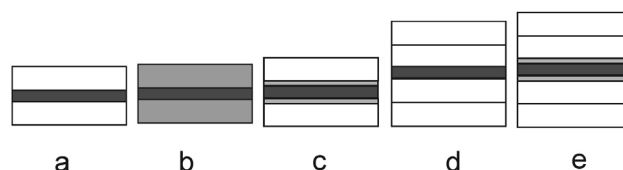
Schematic representation of A/E/A, TAAL/E/TAAL and A/AAL/E/AAL/A are given on Fig. 1a, b and c respectively.

#### 2.2.5. 2A/E/2A and 2A/AAL/E/AAL/2A symmetrical cells

In order to separate the influence of the addition of the anodic anode layer and the influence of an increase of the anode thickness, symmetrical assemblies, in which two successive tapes of anode slurry of 800 μm are cast onto the electrode tape cast at 100 μm. The corresponding symmetrical assembly is noted 2A/E/2A and its realization is schematized on Fig. 1d. In the same manner, assemblies are realized by casting successively onto the electrolyte tape an AAL tape, cast a 100 and 150 μm, respectively, and two successive anode layers of 800 μm. The corresponding symmetrical assembly is noted 2A/AAL/E/AAL/2A and its realization is schematized on Fig. 1e.

2.2.6. Addition of a nickel collecting layer

In some cases and in order to check the validity of these measurements, and also to avoid false interpretations due to current

Fig. 1. Schematic representation of the different assemblies A/E/A (a), TAAL/E/TAAL (b), A/AAL/E/AAL/A (c), 2A/E/2A (d), and 2A/AAL/E/AAL/2A (e). The white, grey and black layers correspond to the anode, active anodic and electrolyte layers, respectively.
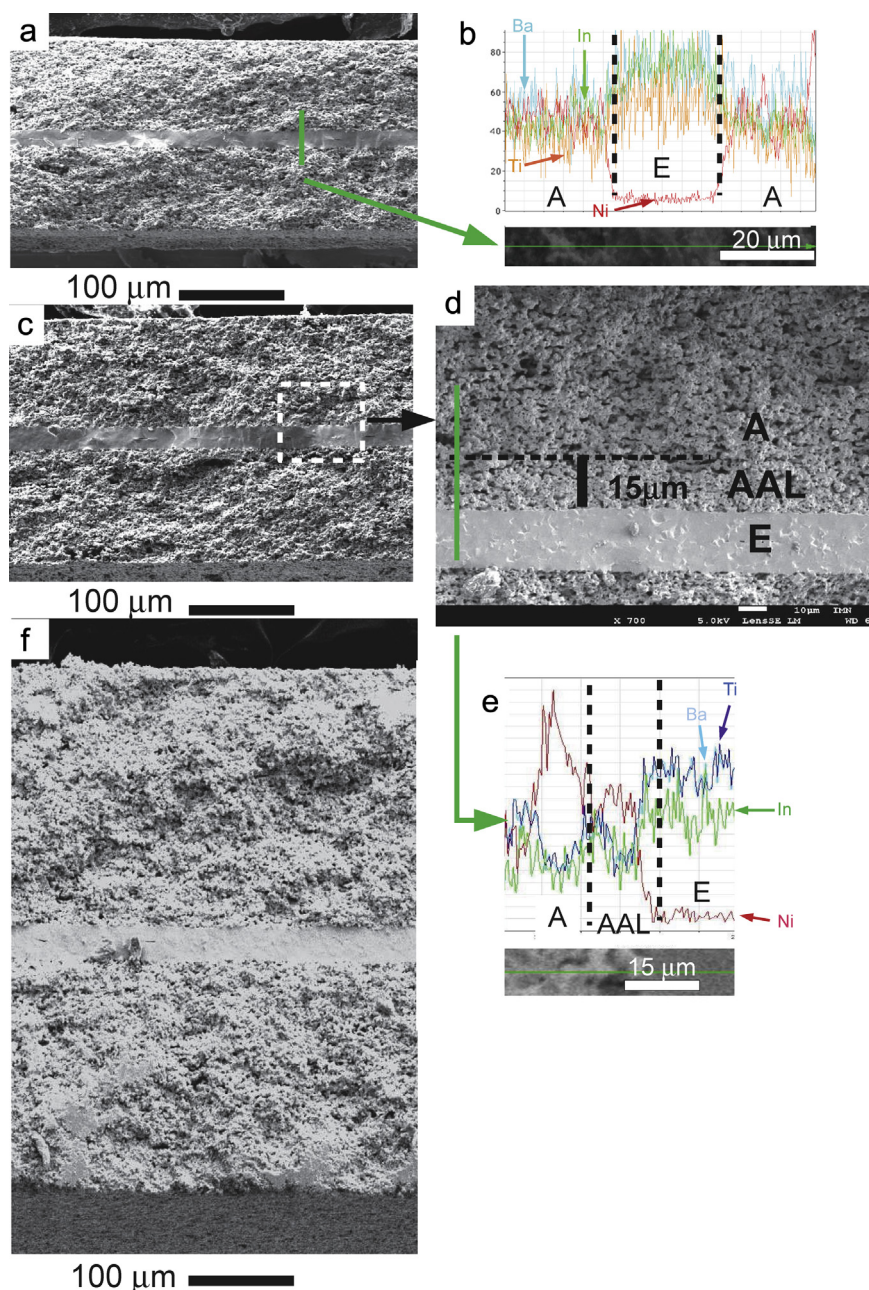
Fig. 2. SEM observations of the cross-section of assemblies: A/E/A (a), A/AAL/E/AAL/A, (c and d) and 2A/E/2A (f), and analysis of the composition obtained by EDX of the interface areas of A/E/A (b) and A/AAL/E (e).

collection defaults, electrochemical impedance spectroscopy (EIS) experiments were performed on assemblies covered with screen printed nickel ink onto the two anode external sides. The ink was prepared by mixing 60 wt.% of Ni (Alfa Aesar) with 40 wt.% of a mixture prepared with terpineol 95 wt.% and ethyl cellulose 5 wt.%.

2.3. Microscopy studies

The morphology of the different compounds and the quality of the different interfaces have been observed by scanning electron spectroscopy (SEM) performed on a JEOL 7600 apparatus equipped with an X-ray analyser for energy-dispersive X-ray spectroscopy (EDX).

2.4. Electrochemical performance of the anode/electrolyte assembly

Gold grids (wire diameter 60 μm, grid opening 250 μm) were placed on the two external sides of the symmetrical cells. Then cells have been reduced at 750 °C for 5 h under wet (3% H_2O) Ar/H_2 (95/5%) atmosphere in order to reduce the NiO to Ni. They then have been tested by EIS under wet (3% H_2O) Ar/H_2(95/5%) atmosphere at different temperatures. The spectrum has been recorded at Udc = 0 V, with a signal amplitude of 50 mV and with 89points scattered in a frequency range from 1 MHz to 0.1 Hz, with a frequency response analyser Solartron 1260. It has been checked that the amplitude of the perturbation signal is small enough to meet the linearity requirement of the transfer function [25]. The data

acquired from the impedance measurements were analysed using ZView2-Software [26].

The evolution of the electrochemical performance versus time was studied using symmetrical half cells maintained at 700 °C for 150 h. Impedance spectra were recorded every 5 h.

3. Results and discussion

3.1. Scanning electron microscopy and energy dispersive X-ray analysis

Fig. 2 shows the cross-sectional SEM micrographs of the different assemblies after final sintering at 1300 °C during 9 h, and the reduction step under wet Ar/H$_2$ atmosphere. The different thicknesses measured by microscopy are given in Table 1. Fig. 2a shows the good quality of the two A/E interfaces, and the rather good adhesion between the two tapes of the electrolyte. The morphology of the two components, very dense for the electrolyte, and rather porous for the anode, is also visible. Analysis of composition obtained by EDX of the interface area, shown in Fig. 2b, confirms a clear phase boundary and the absence of Ni diffusion from anode to electrolyte.

Fig. 2c is rather similar to Fig. 2a, with a good quality of the AAL/E interface. The anode is composed of two distinct layers: (i) an AAL layer (15 μm) connected with the electrolyte (Fig. 2d) and appearing less porous than the anode support, in accordance with the smaller amount of CB introduced during the preparation of the corresponding slurry and (ii) the less dense anode layer (100 μm). The quality of the AAL/E interface is comparable to one observed for the A/E Interface. Our results seem different from the observations of Bi et al. [20], who have shown that the addition of a BaZr$_{0.4}$Ce$_{0.4}$Y$_{0.2}$O$_{3-\delta}$ (BZCY)-NiO AAL anode functional layer between a BZCY electrolyte and a BZCY-NiO anode leads to an increase of the quality of contact between the electrolyte and the anode interface, resulting in an increase of the real contact surface between the anode and the electrolyte. Analysis of composition and elemental distribution mapping using EDX of the interface area, shown in Fig. 2e, confirms that the AAL layer exhibits an average intermediate composition between the one of the anode and of the electrolyte layers. As already observed for the A/E/A assembly, the absence of Ni diffusion from anode to electrolyte is also confirmed for the A/AAL/E/AAL/A assembly.

Fig. 2f shows the morphology of the complete 2A/E/2A assembly. Once again, the quality of the different interfaces is good, and the connexion between the two anode layers cast successively does not appear.

3.2. Electrochemical characterization of the A/E/A assembly

Fig. 3a presents the impedance diagram obtained at 650 °C for the A/E/A assembly. The diagram is mainly composed of three depressed semi-circles and can be fitted by the electrical equivalent circuit L1 + R1 + (R2//CPE2) + (R3//CPE3) + (R4//CPE4) represented on Fig. 3b. The inductance L1 is ascribed to the wires, its value is in the range 0.9–1.1·10^{-6} H, in accordance with literature concerning similar measurements with a similar set-up [27]. The series resistance R1 is attributed to electrolyte, and using its value,
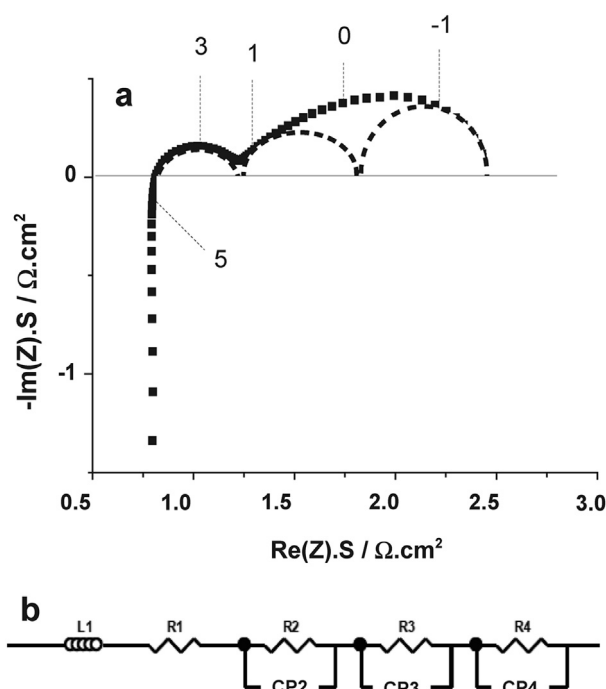

Fig. 3. (a) Nyquist diagram recorded at 650 °C under wet (3% H$_2$O) Ar/H$_2$ (95/5%) atmosphere for the assembly A/E/A. Numbers mentioned above the diagram are the frequency logarithm values. (b) Equivalent circuit used for fitting the impedance diagrams at this temperature.

it is possible to calculate the electrolyte conductivity σ with the formula:

$$\sigma = t/R1S \qquad (1)$$

in which S is the surface area of the electrode and t the thickness of the electrolyte. The value thus obtained is of around 5.10^{-3} S cm^{-1}, i.e. in the range observed for BIT07 pellets with compacities comprised between 80 and 95% [22]. This result also suggests a good quality of the anode/electrolyte interface. Indeed, it is known that in the case of a poor interface, the real contact surface is smaller than the geometrical one, thus the use of this latter in Formula (1) would lead to a conductivity value smaller than the ones measured for pure BIT07 pellets, which is not the case here. The expression of the impedance of the Constant Phase Element (CPE), which often characterize inhomogeneous electrodes, is 1/Q(jω)^n, with an associated capacitance C calculated from the formula (RC)^n = RQ [28,29]. The calculated capacitance values of the R2//CPE2, R3//CPE3 and R4//CPE4 circuits are listed in Table 2. Comparing those values to values reported in previously published studies of similar anode materials used in comparable conditions, it possible to attribute the R2//CPE2 circuit to charge transfer phenomena and R3//CPE3 and R4//CPE4 circuits to diffusion phenomena [20,30–33].

Diagrams were recorded at different temperatures comprised between 300 and 750 °C. As the temperature decreases, the electrolyte contribution to the impedance is no more limited to a series resistance R1, but becomes a depressed arc which can be modelled by an R//CPE circuit as shown in Fig. 4.The corresponding C1 value, which does not depend on temperature and ranges between 10^{-10} and 10^{-11} F cm^{-2}, confirms that this arc is related to the contribution of the BIT07 electrolyte.

The R1 value decreases regularly as the temperature decreases, whereas the corresponding conductivity increases, following an Arrhenius law as shown in Fig. 5 (curve a):

Table 1
Thicknesses, determined by MEB, of the different parts of each assembly.

Name of the assembly	A	AAL	A/AAL	2A	2A/AAL
Ea (μm)	98 ± 3	97 ± 1	111 ± 1	175 ± 6	222 ± 3
Ee (μm)	19 ± 1	27 ± 3	27 ± 2	25 ± 1	20 ± 1

Table 2
Comparison of resistance and capacity values determined from impedance diagrams at 650 °C of A/E/A, AAL/E/AAL, A/AAL/E/AAL/A, 2A/E/2A and 2A/AAL/E/AAL/2A samples.

Sample	R1S (Ω cm [2])	R2S (Ω cm [2])	C2/S (F cm^{-2})	R3S (Ω cm [2])	C3/S (F cm^{-2})	R4S (Ω cm [2])	C4/S (F cm^{-2})
A	0.79	0.42	$12 \cdot 10^{-5}$	0.60	$5.9 \cdot 10^{-2}$	0.69	0.50
TAAL	1.15	0.61	$5 \cdot 10^{-5}$	0.14	$5.2 \cdot 10^{-2}$	–	–
A/AAL	0.98	0.45	$8 \cdot 10^{-5}$	0.19	10^{-2}	0.13	0.16
2A	0.81	0.41	$16 \cdot 10^{-5}$	0.38	$5.1 \cdot 10^{-2}$	1.20	0.15
2A/AAL	0.65	0.36	$19 \cdot 10^{-5}$	0.20	$6.4 \cdot 10^{-2}$	0.97	0.43

$$\sigma = \sigma_0 \exp(-Ea/kT). \tag{2}$$

The value of the activation energy Ea is of 0.67 eV, i.e. in accordance with already published values for BIT07 [22]. C2, C3 and C4 capacities are roughly independent of the temperature, R2 increases strongly when the temperature decreases, as shown on Fig. 6. The variations of R3 and R4 are less regular, with a decrease of R3 and a slight simultaneous increase of R4 when the temperature decreases from 650 °C to 550 °C, and an increase of R3 and a slight decrease of R4 at smaller temperatures. However, as their part in the total resistance becomes less important, it is also more difficult to separate the two corresponding semi-circles observed at low frequencies. These results are in accordance with data of Primdhal et al. [30], in which the resistance of the middle frequency loop is thermally activated, whereas the low frequency loop of the diagram is not dependent on temperature.

In order to evaluate the global performance of the anode assembly it is possible to deduce the area specific resistance (ASR) from the polarization resistance (Rp), which is the sum of R2, R3 and R4 with the formula:

$$ASR = RpS/2, \tag{3}$$

the factor 2 accounting for the fact that the cell is symmetrical. The ASR value at 650 °C is of 0.85 Ω cm^2, and, taking into account the measurement accuracy which can reach 0.1 Ω cm^2, is in accordance with already published results [21]. The variation of the ASR with the temperature, represented on Fig. 7 (curve a), shows an Arrhenius law, with a value of the activation energy Ea of 0.22 eV.

3.3. Electrochemical characterization of the TAAL/E/TAAL assembly

In order to study the influence of the composition of the anode, the TAAL/E/TAAL assembly is compared to the A/E/A one. The impedance diagram obtained for the TAAL/E/TAAL assembly (Fig. 8a) at 650 °C is different from the one obtained for the A/E/A assembly, with, at this temperature, the two loops observed at low frequencies less important and not discernable. The corresponding R and C values, obtained at 650 °C, are given on Table 2. As for A/E/A assembly, it is possible to calculate the ASR, and the corresponding variations, which follow an Arrhenius law with an activation energy of 0.44 eV, are presented on Fig. 7 (curve b). Impedance diagrams recorded at other temperatures show that the low frequencies phenomena are less resistive for all temperatures, but that the increase of R2 values with the decrease in temperature is more important than in the case of the A/E/A assembly. As a result, the comparison of curves a and b of Fig. 7 shows that the ASR values of the TAAL/E/TAAL are smaller for $T > 500$ °C but higher for lower temperatures, in accordance with the differences in the activation energy of the two curves. From the R1 value, it is possible to determine at each temperature the conductivity of the electrolyte, which, taking into account the thickness of the electrolyte, is comparable to results obtained with the A/E/A assembly.

### 3.4. Electrochemical characterization of the A/AAL/E/AAL/A assembly

Fig. 8b shows the impedance diagram of the A/AAL/E/AAL/A assembly at 650 °C. It can be also modelled by the L1 + R1 + (R2// CPE2) + (R3//CPE3) + (R4//CPE4) circuit of Fig. 3b. The corresponding values are given on Table 2. The calculated electrolyte conductivity values are in full agreement with those determined from the A/E/A assembly. This result confirms that, in the contrary to what has been observed by Bi et al. [20], the AAL does not seem to change the surface connected with the electrolyte. The resistance associated to the medium frequencies arc is larger than the two associated to the arcs observed at low frequencies. If the value of R2
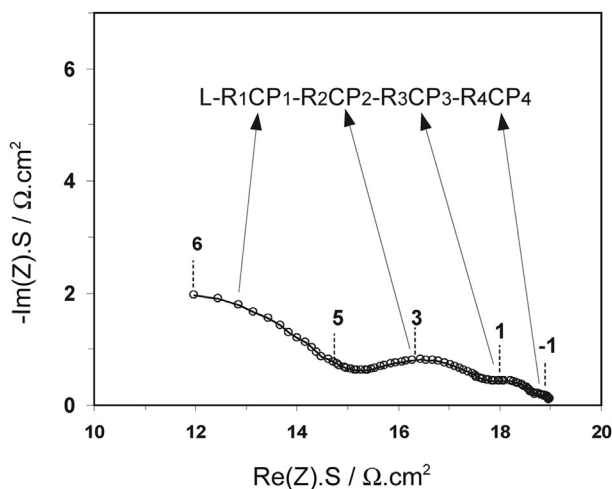
Fig. 4. Nyquist diagram recorded at 400 °C under wet (3% H_2O) Ar/H_2 (95/5%) atmosphere for the assembly A/E/A. Numbers mentioned above the diagram are the frequency logarithm values.
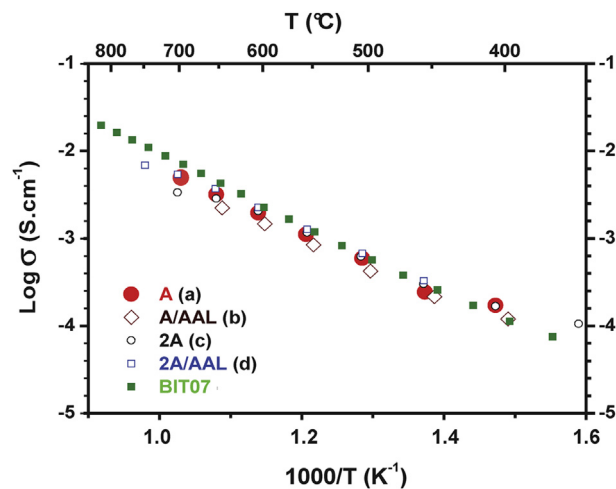

Fig. 5. Arrhenius plots of the BIT07 conductivity calculated from the Nyquist diagrams plotted under wet (3% H_2O) Ar/H_2 (95/5%) atmosphere with A/E/A (a), A/AAL/E/AAL/A (b), 2A/E/2A (c) and 2A/AAL/E/AAL/2A (d) assemblies compared to the conductivity obtained with a BIT07 pellet exhibiting a compacity of 95%.
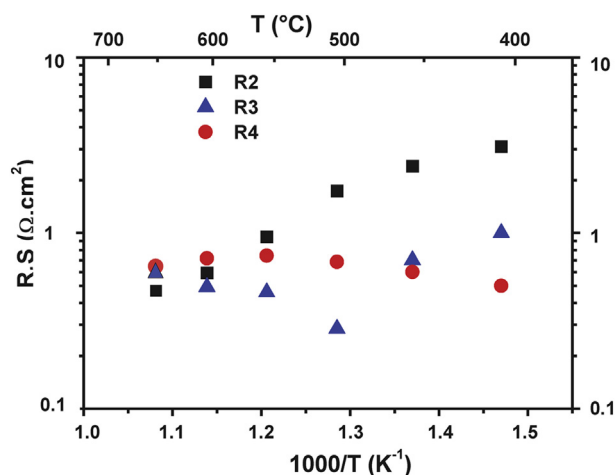
Fig. 6. Temperature evolution of the electrode polarization resistances R2, R3 and R4 measured on the Nyquist diagrams plotted under wet (3% H_2O) Ar/H_2 (95/5%) atmosphere for the A/E/A assembly.

is roughly the same as the value obtained with A/E/A assembly, 0.45 Ω cm^2 instead of 0.42 Ω cm^2, the low frequency resistance is noticeably smaller, leading to a total smaller ASR value. The dense anodic layer with more nickel has an effect on the low frequency phenomena associated with hydrogen adsorption, dissociation and the surface diffusion processes. These results are in accordance with those obtained with YSZ-based cells [34,35], demonstrating that the diffusion processes observed at low frequencies were the rate-determining steps, and depend strongly on all parameter modifying the composition other morphology of the anode, but also on the adjacent functional or collecting layers.

As the temperature decreases, the R1 value decreases, and the associated conductivity values calculated at each temperature (curve b of Fig. 5) are the same as for the A/E/A assembly. Finally, the ASR values of A/AAL/E/AAL/A assembly are smaller than the ASR values of the A/E/A assembly in the entire temperature range, as illustrated in Fig. 7c. The activation energy of the Arrhenius law followed by the variations of the ASR with temperature is of 0.30 eV, i.e. intermediate between the values observed for the A/E/A and TAAL/E/TAAL assemblies.
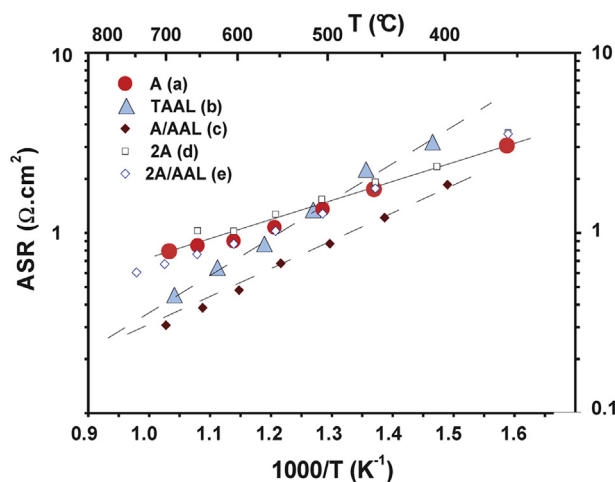
Fig. 7. Temperature evolution of the ASR values measured on the Nyquist diagrams plotted under wet (3% H_2O) Ar/H_2 (95/5%) atmosphere for the A/E/A (a), TAAL/E/TAAL (b), A/AAL/E/AAL/A (c), 2A/E/2A (d) and 2A/AAL/E/AAL/2A (e) assemblies.

3.5. Electrochemical characterization of the 2A/E/2Aand 2A/AAL/E/AAL/2A assemblies

As the addition of the anodic layer AAL leads to an increase of the anode thickness, which can affect the electrode resistance [19,33], the influence of this parameter has been studied with the realization of symmetrical cells for which the anode thickness has been multiplied by 2. Fig. 8c shows the impedance diagram of the 2A/E/2A assembly at 650 °C. It can be fitted by the same equivalent circuit of Fig. 3b, with the corresponding values listed in Table 2. The intersection of the curve with the *x*-axis (R1), taken as the resistance of the electrolyte, leads to BIT07 conductivity values (Curve c of Fig. 5) in agreement with those determined from A/E/A or A/AAL/E/AAL/A cells. Whereas R2 and C2 values are comparable to the values determined for the A/E/A assembly, it is not the case for the two semi-circles observed at low frequencies corresponding to gas diffusion and hydrogen adsorption/dissociation, because the R3//CPE3 circle is smaller, with a smaller R3 value, whereas the R4//CPE4 circle is larger (with also a smaller capacitance value), leading finally to an increase of a total ASR value from 0.85 Ω cm^2 for the A/E/A assembly to 1.00 Ω cm^2 for the 2A/E/2A assembly. This competition between effects resulting from a change in anode thickness has been also observed in other cases [19]. Impedance diagrams were also plotted at other temperatures, and the corresponding variations of the total ASR are shown on Fig. 7d. In this case, the activation energy of the associated Arrhenius law is of 0.21 eV which is not far of 0.22 eV obtained with A/E/A assembly. These results are in accordance with literature generally claiming that above a minimum value, due to a longer path for gas diffusion through the anode, the thicker the electrode, the higher the ASR [19,36].

The influence of the addition of an active anode layer on the 2A/E/2A was finally examined (Fig. 8d and Table 2). When comparing 2A/E/2A and 2A/AAL/E/AAL/2A, it seems that the addition of the active anode layer does not bring significant change in the R2 value, but leads to decreases of R3 and R4 values, as in the case of the A/E/A assembly. Diagrams were recorded at different temperatures, and the resulting variations of the ASR with temperature are presented on Fig. 7e, with an activation energy of the associated Arrhenius law of 0.25 eV.

The benefit of the active anodic layer is nevertheless less important for the 2A/E/2A assembly than for the A/E/A assembly, leading to the supremacy of the A/AAL/E/AAL/A assembly in the entire studied temperature range.

3.6. Influence of nickel collecting layer

According to the literature [37–39], the nature of current collectors has a strong influence on the electrochemical performance of symmetrical cells and the increase of contact area between the electrode and current collector can decrease significantly the polarization losses. According to [37], interesting results are obtained by depositing metal mesh or paste onto the external side of the anode, with the best performance obtained with Ni paste, even if a small evolution, due to nickel diffusion, is observed versus time.

Experiments were done by adding nickel ink onto the two external sides of the A/E/A assembly, this assembly is noted Ni/A/E/A/Ni. The nickel layer, screen printed after the sintering step at 1300 °C (Fig. 9a), is porous with small particle sizes compared to the anode, and a good quality of the interface anode/nickel layer (BIT07-Ni/Ni) can be observed. The thickness of the layer is around 17 μm. The addition of this layer does not bring any major modification, as shown in Fig. 9b at 650 °C: similar impedance result as the one observed for the sample A/E/A are obtained. The variations
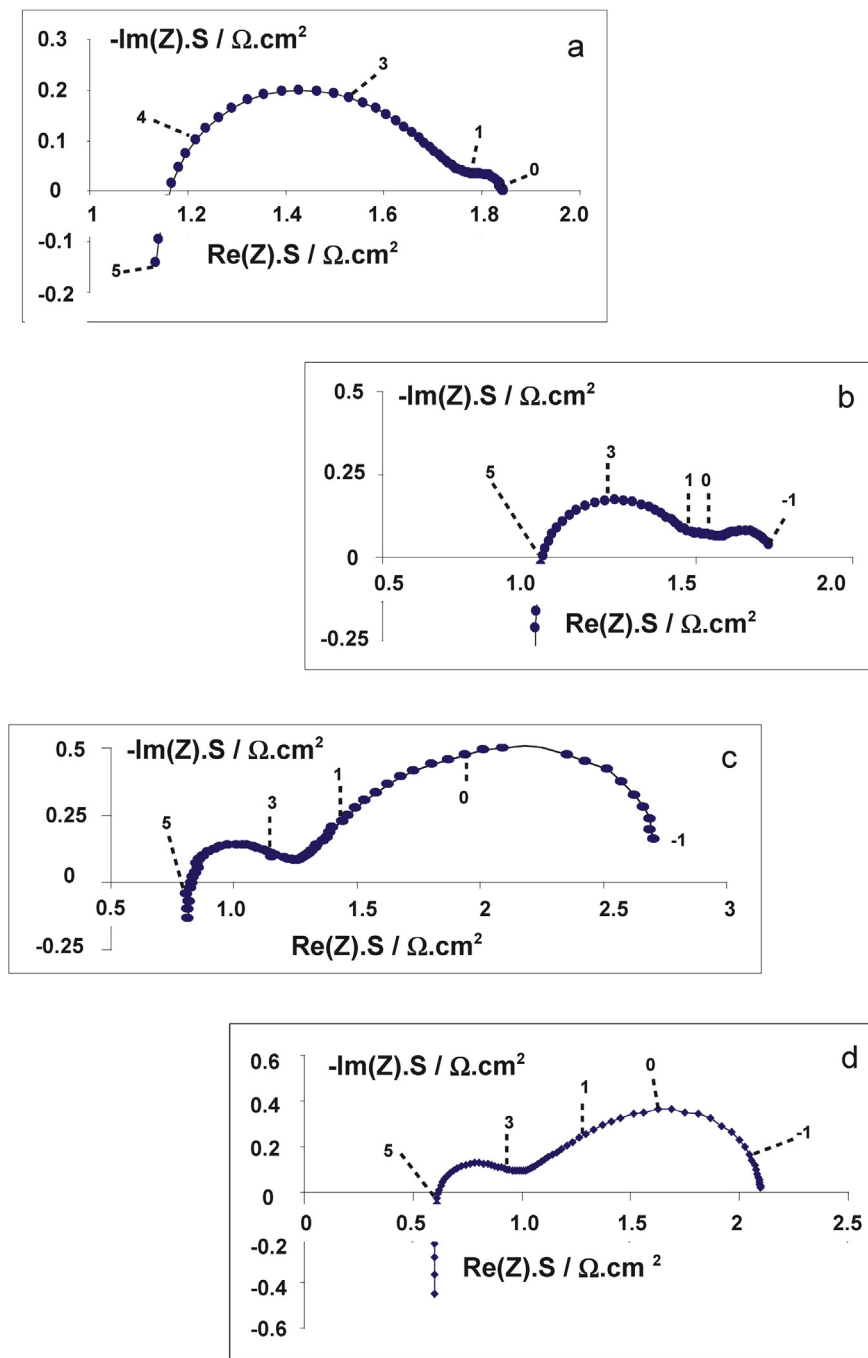
Fig. 8. Nyquist diagram recorded at 650 °C under wet (3% H$_2$O) Ar/H$_2$ (95/5%) atmosphere for the TAAL/E/TAAL(a), A/AAL/E/AAL/A(b), 2A/E/2A (c) and 2A/AAL/E/AAL/2A (d) assemblies. Numbers mentioned above the diagram are the frequency logarithm values.

of the ASR with temperature are similar for the A/E/A and Ni/A/E/Ni assemblies, with the same activation energy of 0.22 eV. Additional experiments were realized by adding nickel ink onto the two external sides of the TAAL/E/TAAL, A/AAL/E/AAL/A, 2A/E/2A and 2A/AAL/E/AAL/2A assemblies. The variations of the ASR with temperature are similar for the two TAAL/E/TAAL and Ni/TAAL/E/TAAL/Ni assemblies with the same activation energy of 0.44 eV and for the A/AAL/E/AAL/A and Ni/A/AAL/E/AAL/A/Ni assemblies, with the same activation energy of 0.30 eV. In these cases, we can assume that the anode performance is not modified by the current collector. The conclusions are the same when comparing 2A/E/2A with

Ni/2A/E/2A/Ni, and 2A/AAL/E/AAL/2A and Ni/2A/AAL/E/AAL/2A/Ni assemblies, with no influence of the nickel layer on the results.

3.7. Ageing experiment

In order to complete the validation of the use of an anodic layer, but also of the current collecting layer, the time evolution of some assemblies has been studied under wet (3% H$_2$O) Ar/H$_2$ 95/5% atmosphere at 700 °C. Curve a of Fig. 10 shows that the ASR of the A/E/A assembly increases regularly, as already observed [21]. Curve b shows that, even if the addition of metal paste as current collector is
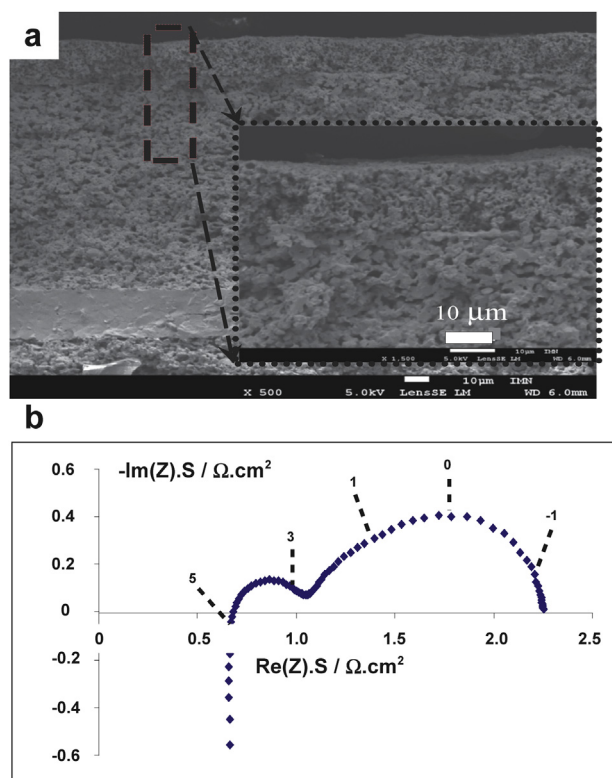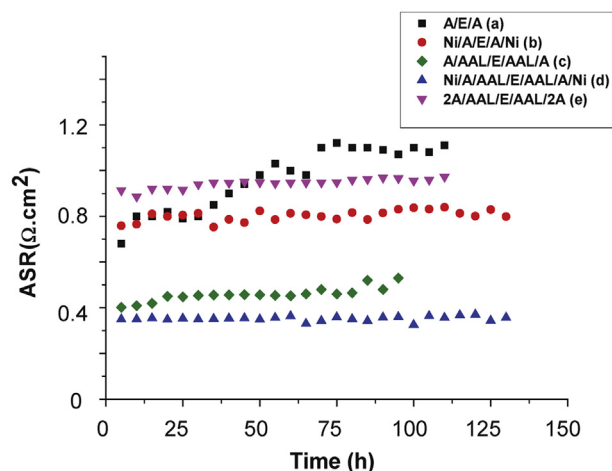
Fig. 9. SEM image of the cross-section of A/E/A assembly with a Ni current collecting layer (a), and Nyquist diagrams recorded at 650 °C under wet (3% H_2O) Ar/H_2 (95/5%) atmosphere for the Ni/A/E/A/Ni. Numbers mentioned above the diagram are the frequency logarithm values.

known to generate small variations (0.02% h^{-1}) due to the diffusion of metal [39], the presence of the current collecting Ni layer improves drastically the ageing of the Ni/A/E/A/Ni assembly. Indeed, during the first 125 h, the ASR variation remains smaller than 0.1% h^{-1}, whereas the ASR variation is 8 times larger for the A/E/A assembly (0.8% h^{-1}).

Even if the ASR of the A/AAL/E/AAL/A assembly increases with time, the active anodic layer improves the ageing of the cell, the degradation speed remaining in this case of 0.2% h^{-1} instead of 0.8% h^{-1} observed for A/E/E. The Ni/A/AAL/E/AAL/A/Ni assembly is

the best one, benefiting from both the improvements brought by the Ni current collecting layer and the active anodic layer. By plotting curve e corresponding to the 2A/AAL/E/AAL/2A assembly, it has been finally checked that the anodic active layer slows down the ageing of the symmetrical cell independently of the thickness of the anode. Nevertheless, taking into account the supremacy of results obtained with thinner anodic layers, ageing experiments were not realized for the Ni/2A/AAL/E/AAL/2A/Ni sample.

4. Conclusion

Symmetrical cells based on BIT07-Ni anode/BIT07 electrolyte using an anode active layer at the anode/electrolyte interface were successfully fabricated using tape casting and co-sintering. The presence of this active layer (≈ 15 μm), which is less porous and contains more nickel particles than the anode cermet, improves the electrochemical performance of the cells by accelerating the electrochemical reactions at the anode/electrolyte interface, and results in a decrease of the cells ASR. This result demonstrates the importance of the anode microstructure near the electrolyte. It has also been proven that this effect is not related to the increase of the anode thickness. Indeed, in our case, an increase of the anode thickness leads to a decrease of the electrochemical performance. Nevertheless the interesting effect of the anodic active layer has also been demonstrated for thicker anodes. Adding a current collecting Ni layer on the external sides of the assemblies does not significantly decrease ASR values, but improves drastically the ageing behaviour of the different cells. Additional studies are now in progress to optimize the composition and the thickness of the active anode layer and to demonstrate its advantage when used in complete solid oxide fuel cells.

References

[1] B.C.H. Steele, Nature 400 (1999) 619–621.
[2] D. Prakash, T. Delahaye, O. Joubert, M.T. Caldes, Y. Piffard, J. Power Sources 167 (2007) 111–117.
[3] J.H. Son, S.I. Park, J.H. Lee, H.S. Kim, J. Mater. Process. Technol. 198 (2008) 414–418.
[4] M. Rieu, P.K. Patro, T. Delahaye, E. Bouyer, Int. J. Appl. Ceram. Technol. 9 (2012) 1049–1057.
[5] Z. Wang, J. Qian, J. Cao, S. Wang, T. Wen, J. Alloys Compd. 437 (2007) 264–268.
[6] M.R. Somalu, V. Yufit, D. Cumming, E. Lorente, N.P. Brandon, Int. J. Hydrogen Energy 36 (2011) 5557–5566.
[7] C. Ding, T. Hashida, Int. J. Hydrogen Energy 36 (2011) 5567–5573.
[8] D.H. Jeon, J.H. Nam, C.J. Kim, J. Electrochem. Soc. 153 (2006) A406–A417.
[9] J.E. Hong, T. Inagaki, S. Ida, T. Ishihara, Int. J. Hydrogen Energy 36 (2011) 4632–4642.
[10] C.X. Li, C.J. Li, L.J. Guo, Int. J. Hydrogen Energy 36 (2011) 2964–2969.
[11] M. Letilly, O. Joubert, A. Le Gal La Salle, J. Power Sources 206 (2012) 210–214.
[12] H. Fukunaga, M. Ihara, K. Sakaki, K. Yamada, Solid State Ionics 86–88 (1996) 1179–1185.
[13] V. Sarıboğa, F. Öksüzömer, Appl. Energy 93 (2012) 707–721.
[14] H. Moon, S.D. Kim, E.W. Park, S.H. Hyun, H.S. Hyun, Int. J. Hydrogen Energy 33 (2008) 2826–2833.
[15] R.J. Gorte, J.M. Vohs, Curr. Opin. Colloid Interface Sci. 14 (2009) 236–244.
[16] M. Brown, S. Primdahl, S. Mogensen, J. Electrochem. Soc. 147 (2000) 475–485.
[17] R.E. Williford, L.A. Chick, G.D. Maupin, S.P. Simner, J.W. Stevenson, J. Electrochem. Soc. 150 (2003) A1067–A1072.
[18] C.W. Tanner, K.Z. Fung, A.V. Virkar, J. Electrochem. Soc. 144 (1997) 21–30.
[19] Y.M. Park, H.J. Lee, H.Y. Bae, J.S. Ahn, H. Kim, Int. J. Hydrogen Energy 37 (2012) 4394–4400.
[20] L. Bi, E. Fabbri, E. Traversa, Electrochem. Commun. 16 (2012) 37–40.
[21] M. Letilly, O. Joubert, M. Caldes, A. Le Gal La Salle, Int. J. Hydrogen Energy 37 (2012) 4346–4355.
[22] A. Le Gal La Salle, M. Letilly, E. Quarez, M. Caldes, O. Joubert, J. Power Sources 196 (2011) 10576–10583.
[23] M.P. Albano, L.B. Garrido, K. Plucknett, L.A. Genova, Ceram. Int. 35 (2009) 1783–1791.
[24] A. Faes, Z. Wuillemin, P. Tanasini, N. Accardo, S. Modena, H.J. Schindler, M. Cantoni, H. Lübbe, S. Diethelm, A. Hessler-Wyser, J. Van Herle, J. Power Sources 196 (2011) 8909–8917.
[25] Q.A. Huang, R. Hui, B. Wang, J. Zhang, Electrochim. Acta 52 (2007) 8144–8164.

Fig. 10. Time evolution of the ASR of the A/E/A (a), Ni/A/E/A/Ni (b), A/AAL/E/AAL/A (c), Ni/A/AAL/E/AAL/A/Ni (d) and 2A/AAL/E/AAL/2A (e) assemblies.

[26] D. Johnson, ZView: A Software Program for IES Analysis, Version 2.8, Scribner associates, INC, Southern Pines, NC, 2002.

[27] D. Marrero-Lopez, J. Pena-Martinez, J.C. Ruiz-Morales, M. Gabas, P. Nunez, M.A.G. Aranda, Solid State Ionics 180 (2010) 1672–1682.

[28] K.S. Cole, R.H. Cole, J. Chem. Phys. 9 (1941) 341–351.

[29] J.R. MacDonald, Impedance Spectroscopy Emphasizing Solid Materials and Systems, Wiley, New York, 1987.

[30] S. Primdahl, M. Mogensen, J. Electrochem. Soc. 144 (1997) 3409–3419.

[31] R. Barfod, M. Mogensen, T. Klemensø, A. Hagen, Y.L. Liu, P.V. Hendriksen, J. Electrochem. Soc. 154 (2007) B371–B378.

[32] T. Klemensø, K. Thydén, M. Chen, H.J. Wang, J. Power Sources 195 (2010) 7295–7301.

[33] U.P. Muecke, K. Akiba, A. Infortuna, T. Salkus, N.V. Stus, L.J. Gauckler, Solid State Ionics 178 (2008) 1762–1768.

[34] S. Primdahl, M. Mogensen, J. Electrochem. Soc. 145 (1998) 2431–2438.

[35] S. Primdahl, M. Mogensen, J. Electrochem. Soc. 146 (1999) 2827–2833.

[36] F. Zhao, A.V. Virkar, J. Power Sources 141 (2005) 79–95.

[37] M. Guillodo, P. Vernoux, J. Fouletier, Solid State Ionics 127 (2000) 99–107.

[38] S.P. Jiang, J.G. Love, L. Apateanu, Solid State Ionics 160 (2003) 15–26.

[39] Z.H. Bi, J.H. Zhu, J. Electrochem. Soc. 158 (2011) B605–B611.